

Article

Tightly Trapped Atom Interferometer inside a Hollow-Core Fiber

Yitong Song, Wei Li * , Xiaobin Xu, Rui Han, Chengchun Gao, Cheng Dai and Ningfang Song

School of Instrumentation and Optoelectronic Engineering, Beihang University, Beijing 100191, China

* Correspondence: wei_li@buaa.edu.cn

Abstract: We demonstrate a fiber-guided atom interferometer in a far-off-resonant trap (FORT) of 100 μK . The differential light shift (DLS) introduced by the FORT leads to the inhomogeneous dephasing of the tightly trapped atoms inside a hollow-core fiber. The DLS-induced dephasing is greatly suppressed in $\pi/2$ - π - $\pi/2$ Doppler-insensitive interferometry. The spin coherence time is extended to 13.4 ms by optimizing the coupling of the trapping laser beam into a quasi-single-mode hollow-core anti-resonant fiber. The Doppler-sensitive interferometry shows a much shorter coherence time, indicating that the main limits to our fiber-guided atom interferometer are the wide axial velocity distribution and the irregular modes of the Raman laser beams inside the fiber. This work paves the way for portable and miniaturized quantum devices, which have advantages for inertial sensing at arbitrary orientations and in dynamic environments.

Keywords: atom interferometer; hollow-core photonic crystal fiber; quantum sensing

1. Introduction

A hollow-core photonic crystal fiber (HC-PCF) [1–4] is a novel type of microstructured optical fiber that guides laser beams in air for transmission. Inside the HC-PCF, the diffraction-free and low-loss light field provides an ideal platform for long-distance, transportable, and enhanced atom–photon interactions. Based on the platform, the frontiers of quantum information technology have developed rapidly, including precision spectroscopy [5], Rydberg atoms [6,7], quantum memories [8,9], and quantum computing [10]. This makes the fiber-guided atom interferometer a promising candidate for portable and miniaturized quantum devices.

Compared to atom interferometers in free space [11,12], fiber-guided atom interferometers have potential in applications such as inertial sensing at arbitrary orientations or in highly dynamic environments as a relatively deep FORT can tightly trap laser-cooled atoms in the radial direction [13]. For instance, a 100 μK FORT inside a hollow-core fiber with a mode-field diameter of 20 μm provides a potential barrier, corresponding to the maximum acceleration of approximately 1000 m/s^2 [14]. Currently, an inertia-sensitive atom interferometer inside the HC-PCF has been realized [15]. However, the severe decay regarding the contrast is mainly due to the inhomogeneous broadening of the DLS between the hyperfine ground-state energy levels. This substantially limits the development of fiber-guided atom interferometers.

To date, several methods have been demonstrated to be effective in canceling the DLS. Our previous study showed the suppression of the DLS in microwave Ramsey interferometry by introducing a weak compensation laser beam into the HC-PCF, whose frequency is tuned in between two hyperfine levels of atoms [16]. However, the method of optical compensation [17] is limited by the mode mismatching of laser beams of different wavelengths inside the HC-PCF and the fluctuations in optical power. Another method compensates for the DLS by implementing an additional magic magnetic field along the elliptically polarized trapping laser beam. The equivalent magnetic field generated by the trapping laser beam will induce a Zeeman shift for the clock transition. Normally, the method of Zeeman-like compensation [18,19] requires a strong external magnetic



Citation: Song, Y.; Li, W.; Xu, X.; Han, R.; Gao, C.; Dai, C.; Song, N. Tightly Trapped Atom Interferometer inside a Hollow-Core Fiber. *Photonics* **2024**, *11*, 428. <https://doi.org/10.3390/photonics11050428>

Received: 19 March 2024

Revised: 26 April 2024

Accepted: 2 May 2024

Published: 3 May 2024



Copyright: © 2024 by the authors. Licensee MDPI, Basel, Switzerland. This article is an open access article distributed under the terms and conditions of the Creative Commons Attribution (CC BY) license (<https://creativecommons.org/licenses/by/4.0/>).

field of a few Gauss at the expense of a large magnetic-field sensitivity and high coils power consumption. In addition, to minimize the DLS-induced dephasing, an approach for cooling atoms directly inside the HC-PCF has been proposed. The in-fiber cooling allows a shallow FORT of a few hundred nano-Kelvin in the interferometry to reduce the DLS and improve the interferometer time up to 20 ms [20]. However, a relatively shallow FORT cannot provide a sufficient potential barrier. This makes fiber-guided atom interferometers lose the advantages in the field of inertial sensing at arbitrary orientations and dynamic environments.

In this paper, we report on a tightly trapped atom interferometer inside a hollow-core fiber and the extension of the interrogation times to tens of milliseconds in a relatively deep FORT. This is achieved because we reverse the DLS-induced inhomogeneous dephasing by optimizing the coupling of the trapping laser beam into a quasi-single-mode hollow-core anti-resonant fiber (HC-ARF) [2–4].

2. Apparatus

As shown in Figure 1a, an HC-ARF is vertically mounted inside a titanium alloy chamber with a vacuum degree of 2.1×10^{-8} Pa. Figure 1b illustrates the frequency configuration of all the laser beams discussed in this paper. In a magneto-optical trap (MOT), the cooling and repump laser beams have a waist radius of 8.0 mm after beam expansion. In addition, we use the same polarization-maintaining single-mode fiber (PM-SMF) and collimation to perform the Gaussian beam shaping of the other laser beams interacting with the ^{87}Rb atoms inside the HC-ARF. The laser beams are then coupled from the bottom of the vacuum chamber into the HC-ARF, and the coupling efficiency is more than 70%. The laser beams leaving from the HC-ARF are split into two optical paths by the non-polarizing beam splitter (NPBS): one for detection and the other for retro-reflection. In the detection optical path, an avalanche photodetector (Thorlabs APD130A) is used to detect the transmission power of the probe laser beams. The trapping laser beam is absorbed and attenuated by a bandpass filter with a center wavelength of 780 nm and an optical density of more than 5. In the retro-reflection optical path, a shortpass dichroic mirror is used to separate laser beams by transmitting and reflecting light at a cutoff wavelength of 805 nm to prevent the superposition of 852 nm laser beams (referred to as the trapping laser beams) propagating in opposite directions inside the HC-ARF. Moreover, the retro-reflected Raman laser pulses of 780 nm are then re-coupled into the HC-ARF by adjusting another mirror.

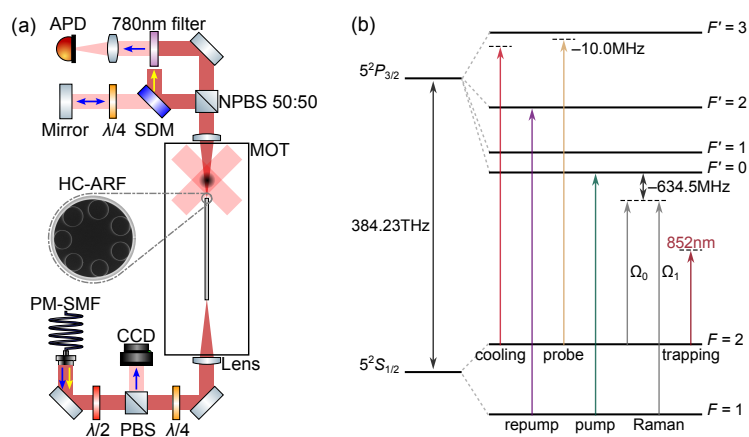


Figure 1. Experiment details: (a) diagram of the experimental system. PM-SMF, polarization-maintaining single-mode fiber; CCD, charge-coupled device camera; PBS, polarizing beam splitter; NPBS, non-polarizing beam splitter; MOT, magneto-optical trap; SDM, shortpass dichroic mirrors; APD, avalanche photodetector. The APD is used to detect the transmission power of the probe laser pulses. The blue and yellow arrows correspond to 780 nm and 852 nm laser beams, respectively; (b) ^{87}Rb D2 transition hyperfine structure and frequency configurations of the laser beams.

3. Results and Discussion

In this paper, a three-pulse Mach–Zender interferometer ($\pi/2-\pi-\pi/2$) is configured as a gravimeter with Raman laser pulses along the HC-ARF. The typical time sequence of the interferometry experiment is shown in Figure 2a, including the processes of building, loading, pump, interferometry, and detection. We next discuss the experimental details and results of the tightly trapped atom interferometer inside the HC-ARF.

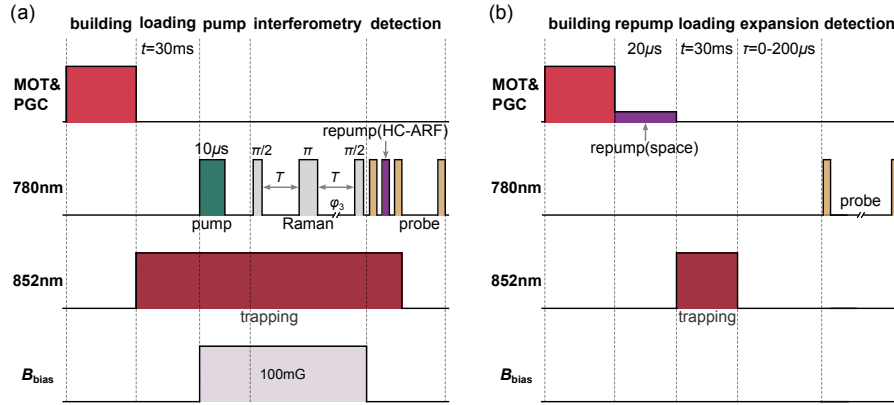


Figure 2. Time sequence: (a) in the interferometry experiment, the laser-cooled atoms inside the HC-ARF are trapped radially by the the 852 nm laser beam; (b) in the experiment of measuring the radial temperature of the atomic cloud, the 852 nm laser beam needs to be turned off before detecting the optical depth of different expansion times τ .

In a $\pi/2-\pi-\pi/2$ interference sequence (i.e., spin-echo sequence), the population-inverting π pulses can theoretically reverse the inhomogeneous dephasing introduced by the DLS. In this case, the normalized population in $|F = 2\rangle$ reads as follows [21]:

$$P_{F=2} = A\{1 - C \cdot \cos[(\langle\delta_1\rangle - \langle\delta_2\rangle) \cdot T + k_e \cdot gT^2 + (\phi_3 - 2\phi_2 + \phi_1)]\}, \quad (1)$$

where A and C represent the amplitude and the contrast regarding the interference fringes, respectively. k_e represents the effective wave vector, and g denotes the component of gravity along HC-ARF. ϕ_1 , ϕ_2 , and ϕ_3 refer to the phases of three pairs of Raman laser pulses. $\langle\delta_i\rangle$ denotes the average detuning of ^{87}Rb atoms during the i -th interrogation time T :

$$\begin{cases} \langle\delta_1\rangle = \delta + \langle\delta v_{z1}\rangle + \langle\delta v_1\rangle \\ \langle\delta_2\rangle = \delta + \langle\delta v_{z2}\rangle + \langle\delta v_2\rangle' \end{cases} \quad (2)$$

where δ is the two-photon Raman detuning. $\langle\delta v_{zi}\rangle$ and $\langle\delta v_i\rangle$ refer to the average second-order Zeeman shift for the clock transition and the average DLS during the i -th interrogation time T , respectively. Equation (1) indicates that the average DLSs of any atom in two successive interrogation times will cancel each other out ($\langle\delta v_1\rangle - \langle\delta v_2\rangle = 0$), as long as the FORT experienced by the atoms inside the fiber is consistent both in time and space.

3.1. Optimizing the Coupling of the Trapping Laser Beam

To avoid the spatial inhomogeneity of the FORT along the HC-ARF and minimize the DLS, we optimize the coupling of the trapping laser beam into a quasi-single-mode HC-ARF in this paper.

In previous studies related to the guidance of atoms, the mode-field diameter (MFD) of the HC-PCF is usually 5–42 μm [22–25]. As the MFD rises, the atomic cloud has a larger interacting region with the trapping laser beam and the guidance efficiency increases. However, the required optical power of the trapping laser beam, corresponding to the large MFD, also increases under the condition of constant trap depth. In addition, to cover the guidance distance of the atomic cloud, the length of the HC-PCF is usually from a few tens to more than a hundred millimeters [22–25]. Under non-optimal coupling conditions,

a small number of higher-order modes are excited inside the HC-PCF and thus cause intensity modulation along the fiber axis [26]. To overcome this problem, a longer HC-PCF can be used as an effective mode filter since higher-order modes usually have much higher transmission loss than fundamental modes [27]. Considering the above conditions, a 7-core HC-ARF is finally used in this paper. The HC-ARF has a core diameter of $27.0\ \mu\text{m}$, a $1/e^2$ MFD of $20.0\ \mu\text{m}$, and a length of 180 mm. As shown in Figure 3b, the near-field mode profile of the HC-ARF in our experiments can be approximated as quasi-single-mode (see previous work for details of the design and simulation results [16]).

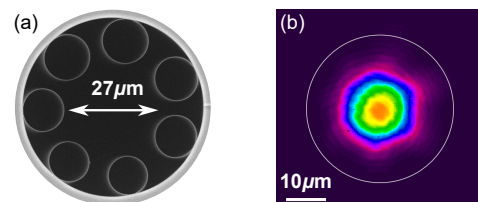


Figure 3. A 7-core hollow-core anti-resonant fiber: (a) microscopic view of the cross-section; (b) the near-field mode profile with $40\times$ magnification. In the pseudo-color image, red and blue colors represent the strongest and weakest optical intensities, respectively.

As shown in Figure 4a, we optimize the coupling of the trapping laser beam into the HC-ARF by adjusting a set of mirrors and an achromatic lens with a focal length of 75 mm. According to the law of Gaussian beam propagation in space, the trapping laser beam leaving from the HC-ARF has a waist of approximately 2 mm after passing through the lens. Figure 4b,c illustrate the far-field mode profiles recorded by a charge-coupled device camera (CCD) during and after the optimization, respectively. Moreover, we evaluate the optimization of the coupling by the overlap integral factor [28,29] between the far-field mode and a standard Gaussian mode with an MFD of 4 mm. The overlap integral factors in Figure 4b,c are 0.948 and 0.986, respectively.

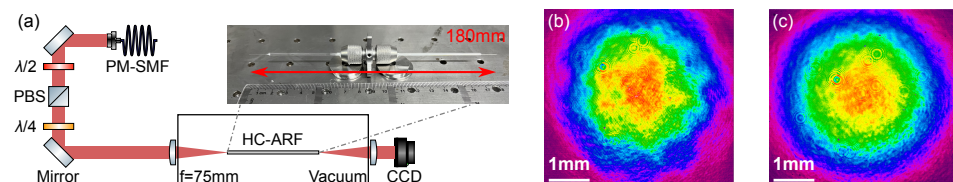


Figure 4. Far-field mode profiles: (a) the setup of the HC-ARF coupling scheme; (b) the far-field mode profile during the optimization; (c) optimized far-field mode profile captured by the CCD.

3.2. Loading of Atoms into the HC-ARF

The atomic cloud is cooled and trapped from rubidium vapor in 1.0 s by an MOT with an efficiency of 5.7×10^8 /s. The cooling laser beam is red-detuned from the ^{87}Rb D2 $|F = 2\rangle \rightarrow |F' = 3\rangle$ transition, while the repump laser beam is resonant on ^{87}Rb D2 $|F = 1\rangle \rightarrow |F' = 2\rangle$ transition. After the 10.0 G/cm gradient magnetic field is turned off, we perform a 25 ms long polarization gradient cooling (PGC). The atomic cloud is further cooled by linearly decreasing the detuning of the cooling laser beam from -18.0 MHz to -100.0 MHz and ramping down the optical power of each laser beam from 10.0 mW to 2.0 mW. Turn off the repump laser beam 1.0 ms before the end of the PGC. Then, the cooling laser beams will pump all the ^{87}Rb atoms to the $|F = 1\rangle$ state. The pushing laser beam, resonant on the ^{87}Rb D2 $|F = 2\rangle \rightarrow |F' = 3\rangle$ transition, is then used to horizontally heat the remaining atoms in the $|F = 2\rangle$ state. After the process of building, the atomic cloud contains approximately 1.0×10^8 at 5.0 μK with an initial diameter of 1.3 mm in the vertical direction.

After turning off the cooling and repump laser beams in MOT, the atomic cloud is freely released from approximately 2.7 mm above the tip of the HC-ARF. We then turn on the 852 nm trapping laser beam to create a FORT that restricts the movement of atoms.

As the atomic cloud expands, many of the atoms are lost. Only a fraction of the atoms that spatially overlap with the trapping laser beam and have temperatures lower than the local FORT are trapped and guided toward the HC-ARF under gravity. As shown in Figure 5a, the darker line indicates the trapped atoms. Since the trapping laser beam is turned on instantaneously, the loading of atoms into the HC-ARF in our experiments is a non-adiabatic process. As the atoms move toward the tip of the HC-ARF, the FORT becomes deeper, resulting in a higher temperature of the atomic cloud. The heating mechanism has been attributed to the transverse compression of the atomic cloud by the funnel-shaped FORT [25] and the intensity modulation from the higher-order modes [26].

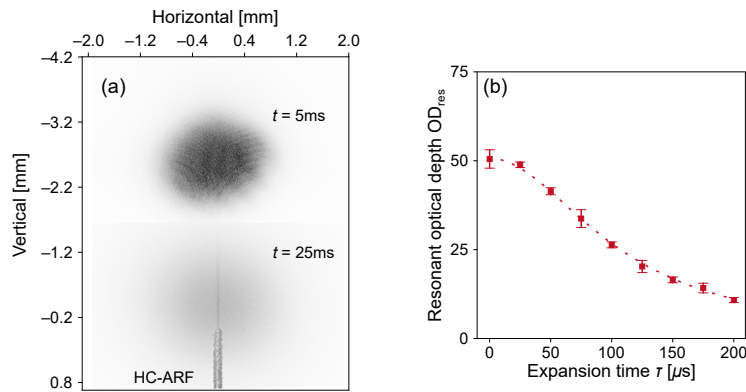


Figure 5. Loading of atoms into the HC-ARF: (a) absorption images of the atomic cloud above the HC-ARF at different loading times t . A coordinate system is established, in which the tip of the HC-ARF is considered as the origin; (b) resonant optical depth OD_{res} versus expansion time τ . Each data point is an average of five repetitions, and the curve is a fit with Equation (4).

We measure the radial temperature of the atomic cloud inside the HC-ARF using the time-of-flight (TOF) method [15,20], and a typical time sequence is shown in Figure 2b. After a loading time t of about 30.0 ms, all the trapped atoms are loaded into the HC-ARF. The trapping laser beam is then turned off, allowing the atomic cloud to expand freely. After an expansion time τ , we send the probe laser pulses to measure the optical depth (OD). The resonant optical depth OD_{res} is calculated as [22]

$$OD_{res}(\tau) \approx OD(\tau)[1 + 4(\delta/\Gamma) + I/I_s], \quad (3)$$

where Γ is the natural linewidth, δ is the detuning of the probe laser pulse, and I and I_s refer to the optical field intensity and saturation intensity, respectively. As shown in Figure 5b, the dashed line is a fit with an equation as follows [30]:

$$OD_{res}(\tau) \approx OD_0 \frac{k_B T / U}{1 + k_B T / U + 4k_B T \tau^2 / (m_a \omega_m)}, \quad (4)$$

where k_B represents the Boltzmann constant, m_a is the atomic mass of ^{87}Rb , ω_m is the waist of the mode-field diameter inside the HC-ARF, OD_0 is the optical depth at the center of the HC-ARF when $\tau = 0$, and U refers to the depth of the FORT. With a trap depth of 100 μK , the radial temperature T of the atomic cloud loaded into the HC-ARF is estimated to be approximately 20 μK . The resonant optical depth OD_{res} when $\tau = 0$ is about 50, corresponding to an atomic number of 5.0×10^4 [22].

3.3. Preparation of Zeeman-Insensitive State

After the process of loading, the ^{87}Rb atoms in the $|F = 1\rangle$ state will be uniformly distributed in three sub-levels $|m_F = 0, \pm 1\rangle$ with a bias magnetic field of 100 mG. In this case, the number of atoms in the Zeeman-insensitive state $|F = 1, m_F = 0\rangle$ is 1/3 of the total number of atoms. To increase the population in the Zeeman-insensitive state, we pump ^{87}Rb atoms to the target sub-level $|m_F = 0\rangle$ using a 10.0 μs long pump laser pulse with

an optical power of tens of nanowatts, resonant on ^{87}Rb D2 $|F = 1\rangle \rightarrow |F' = 0\rangle$ transition. The propagation direction of the pump laser pulse and the direction of the bias magnetic field are both along the HC-ARF. Therefore, the transitions of the ^{87}Rb atoms driven by the pump laser pulse can be decomposed into σ^+ and σ^- transitions, excluding the π transition. Under the transition rules in Figure 6a, the ^{87}Rb atoms in the sub-levels $|m_F = -1\rangle$ and $|m_F = +1\rangle$ are pumped to the Zeeman-insensitive state by the σ^\pm transitions, respectively. In addition, the dipole matrix element for the $|F = 1, m_F = 0\rangle \rightarrow |F' = 0, m_F = 0\rangle$ transition is zero [31]. In this case, the ^{87}Rb atoms in the sub-level $|m_F = 0\rangle$, regarded as a ‘dark state’, no longer interact with the pump laser pulse. Theoretically, all the ^{87}Rb atoms will eventually be distributed in a Zeeman-insensitive state $|F = 1, m_F = 0\rangle$.

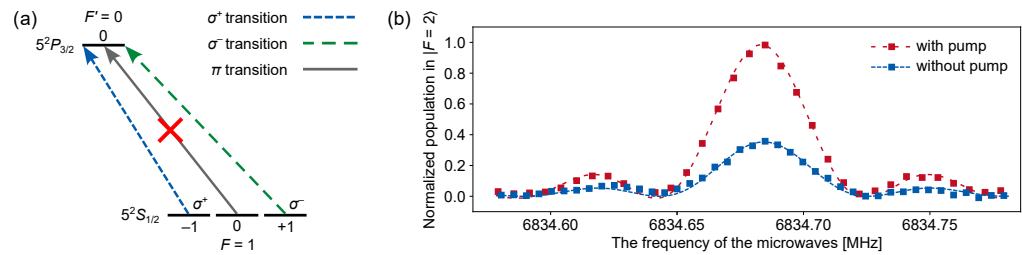


Figure 6. Optical pumping: (a) Zeeman sub-levels of ^{87}Rb and the transition rules. Red cross indicates that the ^{87}Rb atoms in the sub-level $|m_F = 0\rangle$ no longer interact with the pump laser pulse; (b) microwave Raman spectra with and without the pump laser pulse. The measured data points are fitted to the sinc functions.

The pumping efficiency is measured by performing a microwave Raman spectrum. After the pump process, a microwave π pulse with a magnetic field component parallel to the quantization axis and a Rabi frequency of $2\pi \times 25.0$ kHz are applied to pump the atoms from the $|F = 1, m_F = 0\rangle$ state to the $|F = 2, m_F = 0\rangle$ state. For the estimation of the normalized population of the ^{87}Rb atoms, we send three probe laser pulses into the HC-ARF and detect the transmission of these pulses using an APD. All the probe laser pulses have a detuning of -10.0 MHz from the ^{87}Rb D2 $|F = 2\rangle \rightarrow |F' = 3\rangle$ transition, an optical power of 10.0 nW, and a pulse width of 10.0 μs . During the process of detection, the first laser pulse is used to detect the ^{87}Rb atoms in the $|F = 2\rangle$ state. After a repump laser pulse with a pulse width of 5.0 μs , the second laser pulse detects all the ^{87}Rb atoms inside the HC-ARF. As a reference, the third laser pulse detects the optical power after all the ^{87}Rb atoms have been lost. The voltage values V_1 , V_2 , and V_0 converted by the APD correspond to three probe laser pulses, respectively. The normalized population of the ^{87}Rb atoms inside the HC-ARF is calculated as

$$P_{F=2} = \frac{\text{OD}_1}{\text{OD}_2}, \quad (5)$$

where $\text{OD}_1 = -\ln(V_1/V_0)$ and $\text{OD}_2 = -\ln(V_2/V_0)$ refer to the ODs of the ^{87}Rb atoms in the two detection windows. As shown in Figure 6b, the red and blue dashed lines indicate the microwave Raman spectra with and without the pump laser pulse, respectively. After a pump laser pulse, the peak value of the normalized population $P_{F=2}$ increases from about 0.3 to nearly 1.0. Therefore, the pumping efficiency is close to 100%, and the ^{87}Rb atoms in the Zeeman-insensitive state $|F = 1, m_F = 0\rangle$ are approximately 5.0×10^4 with a trap depth of 100 μK .

3.4. Atom Interferometer

3.4.1. Raman Laser Pulses

The Raman laser pulses are generated by a tunable diode laser with a one-photon detuning of $\Delta = -863.67$ MHz from ^{87}Rb D2 $|F = 2\rangle \rightarrow |F' = 2\rangle$ transition. After modulation by an electro-optic modulator (EOM), the sidebands are produced at ^{87}Rb ground-state hyperfine splitting of $\omega_{\text{HFS}} \approx 2\pi \times 6834.68$ MHz. In our experiments, a

pair of Raman laser pulses for a two-photon Raman transition consist of the carrier and the +1-order sideband. However, the −1-order sideband and carrier also create another two-photon Raman transition with opposite phases. The other higher-order pairs are far-detuned, and their contribution to the effective Rabi frequency is negligible. In this case, the effective Rabi frequency Ω_e is approximated as [32]

$$\Omega_e = \frac{\Omega_0\Omega_{+1}}{2\Delta} \frac{\omega_{\text{HFS}}}{\Delta + \omega_{\text{HFS}}} \approx 0.89\Omega_{R+}, \quad (6)$$

where Ω_0 and Ω_{+1} refer to Rabi frequencies of the carrier and the +1-order sideband, respectively. Equation (6) indicates that the effective Rabi frequency of Raman laser pulses in our experiments has a reduction factor of about 0.89. In addition, to cancel out the DLS of ^{87}Rb ground-state hyperfine levels introduced by Raman laser pulses, the power ratio between the carrier P_0 and the +1-order sideband P_1 is configured as follows [33]:

$$\frac{P_0}{P_1} = \frac{\frac{1}{120(\omega_{\text{HFS}}-\Delta_1)} + \frac{1}{8(\omega_{\text{HFS}}-\Delta_2)} + \frac{1}{5(\omega_{\text{HFS}}-\Delta_3)} + \frac{5}{24\Delta_1} + \frac{1}{8\Delta_2}}{\frac{1}{120\Delta_1} + \frac{1}{8\Delta_2} + \frac{1}{5\Delta_3} - \frac{5}{24(\Delta_1+\omega_{\text{HFS}})} - \frac{1}{8(\Delta_2+\omega_{\text{HFS}})}}, \quad (7)$$

where Δ_i refers to the one-photon detuning from the ^{87}Rb D2 $|F = 2\rangle \rightarrow |F' = i\rangle$ transition. According to Equation (7), the power ratio P_0/P_1 of a pair of Raman laser pulses is finally set to 1.72:1 by adjusting the amplitude of the EOM phase modulation.

3.4.2. Doppler-Insensitive Interferometry

Prior to demonstrating a tightly trapped atom interferometer inside the HC-ARF, we perform Doppler-insensitive interferometry to show the upper limit of the coherence time in our experiments by implementing a spin-echo sequence. As shown in Figure 7a, the retro-reflection optical path is blocked, and the direction of the Raman laser pulses is co-propagating in Doppler-insensitive interferometry. The polarization of Raman laser pulses is configured as $\sigma^+-\sigma^+$ by adjusting the quarter-wave plates in Figure 1a. In this case, the effective wave vector experienced by the ^{87}Rb atoms is $(k_1 - k_0)$, corresponding to a gravity sensitivity about five orders of magnitude lower than that of Doppler-sensitive interferometry.

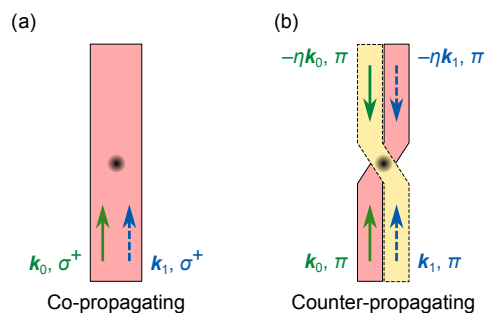


Figure 7. Configuration of Raman laser pulses: (a) co-propagating. The polarization is configured as $\sigma^+-\sigma^+$; (b) counter-propagating. Two pairs of lin \perp lin polarized Raman laser pulses (diagonal and antidiagonal).

The efficiency of the co-propagating Raman laser pulses is estimated by performing Raman spectra inside the HC-ARF. Trapped atoms are pumped from the $|F = 1, m_F = 0\rangle$ state to the $|F = 2, m_F = 0\rangle$ state by a pair of π Raman laser pulses with an effective Rabi frequency of $2\pi \times 9.26$ kHz. Figure 8a,b illustrate the measured normalized population versus the two-photon Raman detunings and Raman pulse durations, respectively. The blue squares in Figure 8 are fitted to a sinc function. The resonance peak of the fitted line shows a shift of approximately $2\pi \times -0.34$ kHz, which corresponds to the average DLS introduced by a 100 μK FORT (see previous work for details [16]). In addition, the red squares in

Figure 8 are fitted to a damped sinusoidal function. The maximum efficiency of a pair of co-propagating Raman laser pulses with a π pulse width of 54.0 μs is approximately 80%.

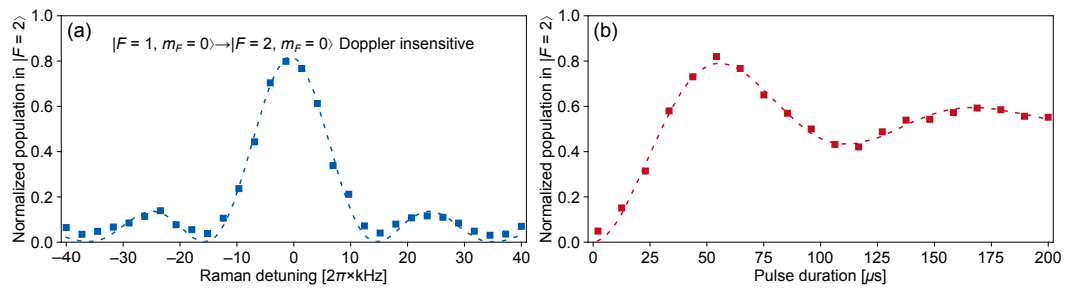


Figure 8. Doppler-insensitive Raman transition: (a) normalized population versus Raman detunings; (b) normalized population versus pulse durations.

After determining the Rabi frequency and the pulse width of the Raman laser pulses, $\pi/2$ - π - $\pi/2$ Doppler-insensitive interferometry is performed inside the HC-ARF. By scanning the phase ϕ_3 of the third $\pi/2$ Raman laser pulses, we observe two Doppler-insensitive interference fringes with interrogation times $2T$ of 2 ms in Figure 9a, corresponding to the far-field mode profiles of the trapping laser beam during and after the optimization, respectively. The contrasts, obtained from the fitting results of the measured data points in Figure 9a according to Equation (1), are 0.59 and 0.28, respectively. Under non-optimal coupling conditions, both the trapping and Raman laser beams excite higher-order modes as the 852 nm and 780 nm laser beams in this paper are coupled into the HC-ARF through the same PM-SMF and optical paths. The red squares in Figure 9a show that the inhomogeneity of the 852 nm laser beam mainly leads to an increase in the residual DLS (or additional phase) and a decay in the contrast C of the interference fringe, while the inhomogeneity of the 780 nm laser beam leads to the inefficiency of the co-propagating Raman laser pulses and a decrease in the amplitude A of the interference fringes. In addition, the blue triangles in Figure 9a suggest that optimizing the coupling of the trapping laser beam is effective in suppressing the DLS caused by the spatial inhomogeneity of the FORT along the fiber.

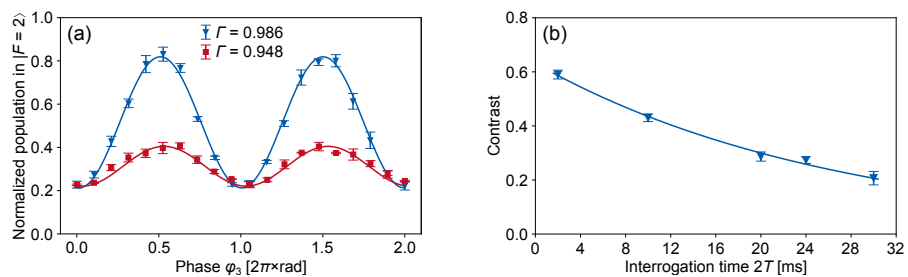


Figure 9. Doppler-insensitive interferometry inside the HC-ARF: (a) interference fringes with interrogation times $2T$ of 2 ms. The red squares and blue triangles correspond to the far-field mode profiles of the trapping laser beam during and after the optimization, respectively. Each data point is an average of three repetitions with the standard deviation; (b) contrast versus interrogation times $2T$ under the condition of optimal coupling. Each data point corresponds to an average of three fitting results from the interference fringes, and the curve is a fit with an exponential decay function [see Equation (8)].

To estimate the coherence time T^* , we further measure Doppler-insensitive interference fringes with different interrogation times $2T$ under the condition of optimal coupling. It is difficult to decouple the residual DLS, the inhomogeneity of the second-order Zeeman shift along the HC-ARF, the intensity fluctuations of the trapping laser beam, and the vibration noise from the laboratory, which cause the decoherence of a $\pi/2$ - π - $\pi/2$ Doppler-insensitive interferometry inside the HC-ARF. In this case, we fit the contrast regarding

the interference fringe in Figure 9b by the usual exponential decay as the interrogation times increase:

$$C(T) = C_0 e^{-T/T^*}, \tag{8}$$

where the coherence time T^* is defined as the time T for the fitted curve to decay to $1/e$ of the maximum contrast C_0 . According to Equation (8), the coherence time T^* of Doppler-insensitive interferometry with a 100 μK FORT is about 13.4 ms, corresponding to interrogation times of $2T = 26.8$ ms. In contrast, the coherence time T^* of the atomic cloud in a $\pi/2$ - $\pi/2$ microwave Ramsey sequence is less than 3.0 ms with the same trap depth of 100 μK (see previous work for details [16]). The experimental results indicate that the inhomogeneous dephasing introduced by the DLS has been effectively reversed in a spin-echo sequence by optimizing the coupling of the trapping laser beam into a quasi-single-mode HC-ARF. In future work, we plan to monitor and stabilize the optical power of the trapping laser beam, replace a uniform bias magnetic field, and use a vibration isolation platform to further extend the upper limit of the coherence time in our experiments.

3.4.3. Doppler-Sensitive Interferometry

Unlike Doppler-insensitive interferometry, the polarization in Doppler-sensitive interferometry is configured as $\text{lin} \perp \text{lin}$ and the direction of Raman laser pulses is counter-propagating, corresponding to an effective wave vector of $(\mathbf{k}_1 + \mathbf{k}_0)$. As shown in Figure 1a, the transmission of NPBS and the re-coupling efficiency of the Raman laser pulse are approximately 45% and 70%, respectively. Therefore, the retro-reflection optical path in our experiments results in an attenuation factor η of approximately 0.14 on the optical power of the incident Raman laser pulse. The counter-propagating Raman spectrum of the ^{87}Rb atoms inside HC-ARF is measured by scanning the two-photon Raman detunings of the Raman laser pulses with a π pulse width of 10.0 μs . Since the polarization extinction ratio of the counter-propagating Raman laser pulses in our experiments is only about 20 dB, one Doppler-insensitive resonance peak with a line width of about 50.0 kHz, which ideally should not exist, can still be observed in Figure 10. As the ^{87}Rb atoms fall along the HC-ARF, the two Doppler-sensitive resonance peaks in the Raman spectrum exhibit opposite shifts, which correspond to the two pairs of counter-propagating Raman laser pulses (diagonal and antidiagonal) in Figure 7b, respectively. At a loading time of t , the Doppler shift $2\omega_D$ between two Doppler-sensitive resonance peaks is calculated as follows:

$$\omega_D = (\mathbf{k}_1 + \mathbf{k}_0) \cdot \mathbf{v}_0(t) \approx 2\mathbf{k}_1 \cdot \mathbf{v}_0(t), \tag{9}$$

where \mathbf{v}_0 represents the center velocity of the atomic cloud. According to Equation (9), the center velocity of the atomic cloud along the HC-ARF at a loading time of $t = 30.0$ ms is about 0.41 m/s. The axial velocity distribution of the atomic cloud inside the HC-ARF introduces Doppler broadening to the counter-propagating resonance peak, resulting in a broadened full width at half maximum (FWHM) of approximately 360 kHz.

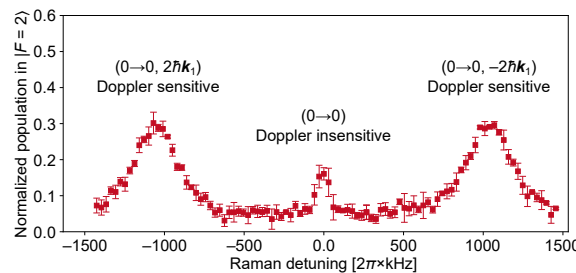


Figure 10. Doppler broadening of Raman transition due to the axial velocity distribution. The error bars are the standard deviation of the average of three experimental runs.

We then perform $\pi/2$ - π - $\pi/2$ Doppler-sensitive interferometry inside the HC-ARF by scanning the phase ϕ_3 of the third $\pi/2$ Raman laser pulses. Figure 11a shows the Doppler-

sensitive interference fringes with different π pulse widths τ_π . Due to Doppler broadening, the Raman laser pulses with a π pulse width of $2.5\ \mu\text{s}$ (red squares) can pump more ^{87}Rb atoms than the Raman laser pulses with a π pulse width of $10.0\ \mu\text{s}$ (blue triangles). The measured data points of the blue triangles and the red squares are fitted with Equation (1), corresponding to contrasts of 0.08 and 0.26, respectively. As shown in Figure 11b, we perform the same atom interferometry at different positions inside the HC-ARF. During the time interval from 30 to 50 ms, the movement range of the atoms is approximately 10.2 mm according to the kinematic equation. With the increase in the loading time t , the phase offset of the interference fringe remains relatively consistent, although the contrast gradually decreases. We also plot Doppler-sensitive interference fringes with different trap depths in Figure 11c. As the dipole trap becomes shallower, the contrast regarding the interference fringes increases due to the decrease in the DLS introduced by the FORT [20] and the lower temperature of the atomic cloud inside the HC-ARF [22].

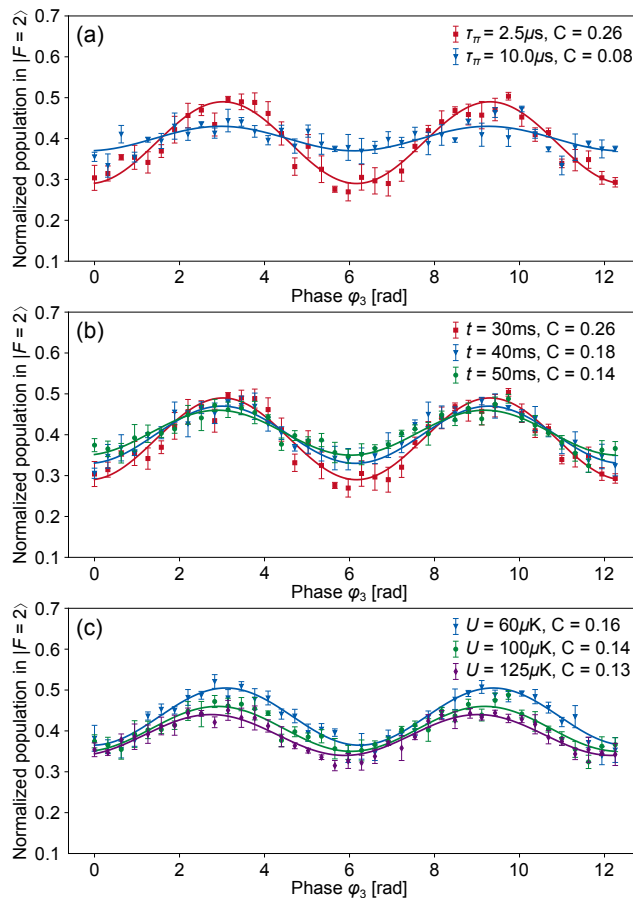


Figure 11. Doppler-sensitive interference fringes: (a) with different π pulse widths τ_π , and interrogation times $2T = 60\ \mu\text{s}$. The error bars are the standard deviation of the average of three repetitions; (b) at different loading times t . The interrogation times are $60\ \mu\text{s}$, and the trap depth is $100\ \mu\text{K}$. The error bars represent the standard deviation of three experimental runs; (c) with different depths U . The interrogation times are $60\ \mu\text{s}$, and the loading time is $50\ \text{ms}$. Each data point is an average of three repetitions with the standard deviation.

To fit the coherence time T^* , we measure Doppler-sensitive interference fringes with different interrogation times $2T$. Figure 12a illustrates the contrast versus interrogation times under the condition of a π pulse width $\tau_\pi = 2.5\ \mu\text{s}$. The coherence time, estimated from the damped curve, is about $43.3\ \mu\text{s}$. Compared to the Doppler-insensitive interferometry, the coherence time of the Doppler-sensitive interferometry is reduced by a factor of several hundred when using the same trap depth of $100\ \mu\text{K}$. This indicates that the

contrast regarding the Doppler-sensitive interference fringes in our experiments is not mainly limited by the residual DLS caused by the trapping laser beam.

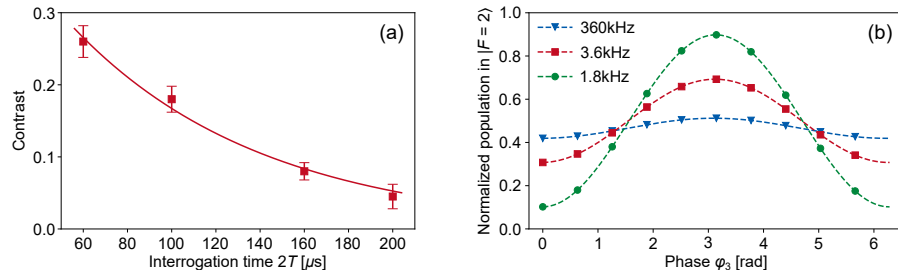


Figure 12. Doppler-sensitive interferometry inside the HC-ARF: (a) contrast versus interrogation times $2T$. Each data point corresponds to an average of three fitting results from the interference fringes, and the damped curve is a fit with Equation (8); (b) interference fringes with different Doppler shifts. The contrasts of the blue triangles, red squares, and green dots are 0.08, 0.39, and 0.79, respectively.

We attribute the decay in the contrast to the inefficiency of the counter-propagating Raman laser pulses. One reason for the inefficiency is the wide axial velocity distribution (or the high axial temperature) of the atomic cloud. In a three-pulse Mach-Zender interferometer, the normalized population in $|F = 2\rangle$ state is calculated as follows [34]:

$$P_{F=2} = \int |M_{\pi/2} M_{\pi} M_{\pi/2} \begin{bmatrix} c_1(t) \\ c_2(t) \end{bmatrix}|^2 \cdot dv, \quad (10)$$

where c_1 and c_2 represent the probability amplitude that the atom is in the $|F = 1\rangle$ and $|F = 2\rangle$ states at time t , respectively. M denotes the matrix corresponding to Raman laser pulses:

$$M = \begin{bmatrix} \cos(\Omega\tau/2) - i \sin(\Omega\tau/2)\delta(v)/\Omega & -ie^{i[\delta(v)t+\phi]} \sin(\Omega\tau/2)\Omega_e/\Omega \\ -ie^{-i[\delta(v)t+\phi]} \sin(\Omega\tau/2)\Omega_e/\Omega & \cos(\Omega\tau/2) + i \sin(\Omega\tau/2)\delta(v)/\Omega \end{bmatrix}, \quad (11)$$

where τ is the Raman laser pulse duration, ϕ is the phase of the Raman laser pulse, $\delta(v)$ is the two-photon Raman detuning due to the Doppler shift, and the axial velocity v is Gaussian-distributed. Ω_e and $\Omega = \sqrt{\Omega_e^2 + \delta^2(v)}$ refer to the effective Rabi frequency and the generalized Rabi frequency, respectively. To demonstrate that the axial velocity distribution is a main obstacle to improving the coherence time, we numerically calculated the Doppler-sensitive interference fringes corresponding to different Doppler shifts according to Equations (10) and (11). The probability amplitudes of the atoms in the $|F = 1\rangle$ state before the three-pulse Raman laser are $c_1(t) = 1$ and $c_2(t) = 0$, respectively. A π Raman laser pulse has a pulse width of $2.5 \mu\text{s}$, and the interrogation times $2T$ are $200 \mu\text{s}$. We then plot the integration results in Figure 12b by scanning the phase ϕ_3 of the last $\pi/2$ Raman laser pulses. The Doppler broadening values of the blue triangles, red squares, and green dots in Figure 12b are 360.0 kHz, 3.6 kHz, and 1.8 kHz, corresponding to contrasts of 0.08, 0.39, and 0.79, respectively. The results of the theoretical calculations illustrate that a wide axial velocity distribution leads to the smearing of the Doppler-sensitive interference fringes.

Another reason for the inefficiency includes the irregular modes of the counter-propagating Raman laser pulses along the HC-ARF. The current setup is designed to optimize the coupling of the 852 nm laser beam. Under non-optimal conditions, a small number of higher-order modes are excited when the 780 nm laser beams are coupled from the bottom into the HC-ARF, as shown in Figure 13a. Moreover, more higher-order modes inside the HC-ARF can be observed after re-coupling the 780 nm laser beams from the top to bottom, as shown in Figure 13b. In this case, the counter-propagating Raman laser pulses cannot produce a constant effective Rabi frequency for the ^{87}Rb atoms.

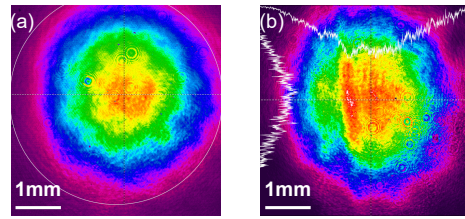


Figure 13. The irregular far-field mode profiles of Raman laser pulses: (a) coupling into the HC-ARF from the bottom; (b) re-coupling from the top to bottom.

4. Conclusions

In conclusion, we have demonstrated a tightly trapped atom interferometer inside the HC-ARF. By optimizing the coupling of the trapping laser beam into a quasi-single-mode HC-ARF, the inhomogeneous dephasing introduced by the DLS is effectively reversed. This optimization results in a coherence time of 13.4 ms in Doppler-insensitive interferometry with a 100 μ K FORT. The significant decay regarding the contrast in the Doppler-sensitive interferometry is primarily attributed to the inhomogeneity of the Raman laser pulses. This issue can be further solved by replacing the HC-ARF with a strong suppression of the higher-order modes [27,35] and employing an achromatic coupling setup for multi-wavelength circumstances. We also expect to suppress the Doppler broadening and improve the efficiency of the Raman laser pulses by atomic velocity selection [36,37] or Raman sideband cooling for tightly trapped atoms [5,38]. Our long-term goal is to enhance the performance of the tightly trapped atom interferometer inside the HC-ARF to the level of Doppler-insensitive interferometry. This would result in an inertial sensitivity (fundamentally limited by the atom shot noise σ_{shot}) of approximately 1.4 mGal/shot with 5×10^4 atoms, $2T = 20$ ms interrogation times, and a contrast of 0.2. Our work establishes an important step towards a fiber-guided atom interferometer that has the potential for inertial sensing at arbitrary orientations and in dynamic environments such as space, airborne, shipborne, and underwater.

Author Contributions: Conceptualization, W.L. and Y.S.; methodology, W.L. and Y.S.; investigation, Y.S. and W.L.; data curation, Y.S., C.G. and C.D.; writing—original draft preparation, Y.S.; writing—review and editing, W.L.; visualization, Y.S., W.L. and R.H.; supervision, N.S., X.X. and W.L.; project administration, N.S., X.X. and W.L.; funding acquisition, N.S. and W.L. All authors have read and agreed to the published version of the manuscript.

Funding: This research was supported by China National Postdoctoral Program for Innovative Talents (BX2021028).

Institutional Review Board Statement: Not applicable.

Informed Consent Statement: Not applicable.

Data Availability Statement: Data underlying the results presented in this paper are not publicly available at this time but may be obtained from the authors upon reasonable request.

Acknowledgments: The authors would like to thank Fei Yu from Shanghai Institute of Optics and Fine Mechanics, Chinese Academy of Sciences for providing the HC-ARF samples.

Conflicts of Interest: The authors declare no conflicts of interest.

References

1. Russell, P. Photonic Crystal Fibers. *Science* **2003**, *299*, 358–362. [[CrossRef](#)] [[PubMed](#)]
2. Poletti, F. Nested Antiresonant Nodeless Hollow Core Fiber. *Opt. Express* **2014**, *22*, 23807. [[CrossRef](#)] [[PubMed](#)]
3. Debord, B.; Amsanpally, A.; Chafer, M.; Baz, A.; Maurel, M.; Blondy, J.M.; Hugonnot, E.; Scol, F.; Vincetti, L.; G er ome, F.; et al. Ultralow Transmission Loss in Inhibited-Coupling Guiding Hollow Fibers. *Optica* **2017**, *4*, 209. [[CrossRef](#)]
4. Sakr, H.; Chen, Y.; Jasion, G.T.; Bradley, T.D.; Hayes, J.R.; Mulvad, H.C.H.; Davidson, I.A.; Numkam Fokoua, E.; Poletti, F. Hollow Core Optical Fibres with Comparable Attenuation to Silica Fibres between 600 and 1100 nm. *Nat. Commun.* **2020**, *11*, 6030. [[CrossRef](#)] [[PubMed](#)]

5. Okaba, S.; Takano, T.; Benabid, F.; Bradley, T.; Vincetti, L.; Maizelis, Z.; Yampol'skii, V.; Nori, F.; Katori, H. Lamb-Dicke Spectroscopy of Atoms in a Hollow-Core Photonic Crystal Fibre. *Nat. Commun.* **2014**, *5*, 4096. [CrossRef]
6. Epple, G.; Kleinbach, K.S.; Euser, T.G.; Joly, N.Y.; Pfau, T.; Russell, P.S.J.; Löw, R. Rydberg Atoms in Hollow-Core Photonic Crystal Fibres. *Nat. Commun.* **2014**, *5*, 4132. [CrossRef]
7. Langbecker, M.; Noaman, M.; Kjærgaard, N.; Benabid, F.; Windpassinger, P. Rydberg Excitation of Cold Atoms inside a Hollow-Core Fiber. *Phys. Rev. A* **2017**, *96*, 041402. [CrossRef]
8. Sprague, M.R.; Michelberger, P.S.; Champion, T.F.M.; England, D.G.; Nunn, J.; Jin, X.M.; Kolthammer, W.S.; Abdolvand, A.; Russell, P.S.J.; Walmsley, I.A. Broadband Single-Photon-Level Memory in a Hollow-Core Photonic Crystal Fibre. *Nat. Photonics* **2014**, *8*, 287–291. [CrossRef]
9. Li, W.; Islam, P.; Windpassinger, P. Controlled Transport of Stored Light. *Phys. Rev. Lett.* **2020**, *125*, 150501. [CrossRef]
10. Venkataraman, V.; Saha, K.; Gaeta, A.L. Phase Modulation at the Few-Photon Level for Weak-Nonlinearity-Based Quantum Computing. *Nat. Photonics* **2013**, *7*, 138–141. [CrossRef]
11. Hu, Z.K.; Sun, B.L.; Duan, X.C.; Zhou, M.K.; Chen, L.L.; Zhan, S.; Zhang, Q.Z.; Luo, J. Demonstration of an Ultrahigh-Sensitivity Atom-Interferometry Absolute Gravimeter. *Phys. Rev. A* **2013**, *88*, 043610. [CrossRef]
12. Fu, Z.; Wang, Q.; Wang, Z.; Wu, B.; Cheng, B.; Lin, Q. Participation in the Absolute Gravity Comparison with a Compact Cold Atom Gravimeter. *Chin. Opt. Lett.* **2019**, *17*, 011204. [CrossRef]
13. Yoon, T.; Bajcsy, M. Laser-Cooled Cesium Atoms Confined with a Magic-Wavelength Dipole Trap inside a Hollow-Core Photonic-Bandgap Fiber. *Phys. Rev. A* **2019**, *99*, 023415. [CrossRef]
14. Schrader, D.; Kuhr, S.; Alt, W.; Müller, M.; Gomer, V.; Meschede, D. An Optical Conveyor Belt for Single Neutral Atoms. *Appl. Phys. B* **2001**, *73*, 819–824. [CrossRef]
15. Xin, M.; Leong, W.S.; Chen, Z.; Lan, S.Y. An Atom Interferometer inside a Hollow-Core Photonic Crystal Fiber. *Sci. Adv.* **2018**, *4*, e1701723. [CrossRef] [PubMed]
16. Song, Y.; Li, W.; Xu, X.; Han, R.; Gao, C.; Dai, C.; Song, N. Suppressing the Dephasing of Optically Trapped Atoms inside a Hollow-Core Fiber. *Opt. Lett.* **2024**, *49*, 206. [CrossRef] [PubMed]
17. Kaplan, A.; Fredslund Andersen, M.; Davidson, N. Suppression of Inhomogeneous Broadening in Rf Spectroscopy of Optically Trapped Atoms. *Phys. Rev. A* **2002**, *66*, 045401. [CrossRef]
18. Carr, A.W.; Saffman, M. Doubly Magic Optical Trapping for Cs Atom Hyperfine Clock Transitions. *Phys. Rev. Lett.* **2016**, *117*, 150801. [CrossRef] [PubMed]
19. Xin, M.; Leong, W.S.; Chen, Z.; Lan, S.Y. Transporting Long-Lived Quantum Spin Coherence in a Photonic Crystal Fiber. *Phys. Rev. Lett.* **2019**, *122*, 163901. [CrossRef]
20. Wang, Y.; Chai, S.; Billotte, T.; Chen, Z.; Xin, M.; Leong, W.S.; Amrani, F.; Debord, B.; Benabid, F.; Lan, S.Y. Enhancing Fiber Atom Interferometer by In-Fiber Laser Cooling. *Phys. Rev. Res.* **2022**, *4*, L022058. [CrossRef]
21. Kuhr, S.; Alt, W.; Schrader, D.; Dotsenko, I.; Miroshnychenko, Y.; Rauschenbeutel, A.; Meschede, D. Analysis of Dephasing Mechanisms in a Standing-Wave Dipole Trap. *Phys. Rev. A* **2005**, *72*, 023406. [CrossRef]
22. Bajcsy, M.; Hofferberth, S.; Peyronel, T.; Balic, V.; Liang, Q.; Zibrov, A.S.; Vuletic, V.; Lukin, M.D. Laser-Cooled Atoms inside a Hollow-Core Photonic-Crystal Fiber. *Phys. Rev. A* **2011**, *83*, 063830. [CrossRef]
23. Vorrath, S.; Möller, S.A.; Windpassinger, P.; Bongs, K.; Sengstock, K. Efficient Guiding of Cold Atoms through a Photonic Band Gap Fiber. *New J. Phys.* **2010**, *12*, 123015. [CrossRef]
24. Hilton, A.; Perrella, C.; Benabid, F.; Sparkes, B.; Luiten, A.; Light, P. High-Efficiency Cold-Atom Transport into a Waveguide Trap. *Phys. Rev. Appl.* **2018**, *10*, 044034. [CrossRef]
25. Langbecker, M.; Wirtz, R.; Knoch, F.; Noaman, M.; Speck, T.; Windpassinger, P. Highly Controlled Optical Transport of Cold Atoms into a Hollow-Core Fiber. *New J. Phys.* **2018**, *20*, 083038. [CrossRef]
26. Wang, Y.; Chai, S.; Xin, M.; Leong, W.S.; Chen, Z.; Lan, S.Y. Loading Dynamics of Cold Atoms into a Hollow-Core Photonic Crystal Fiber. *Fibers* **2020**, *8*, 28. [CrossRef]
27. Uebel, P.; Günendi, M.C.; Frosz, M.H.; Ahmed, G.; Edavalath, N.N.; Ménard, J.M.; Russell, P.S. Broadband Robustly Single-Mode Hollow-Core PCF by Resonant Filtering of Higher-Order Modes. *Opt. Lett.* **2016**, *41*, 1961. [CrossRef] [PubMed]
28. Wu, Y.K.; Wang, W.S. Design and Fabrication of Sidewalls-Extended Electrode Configuration for Ridged Lithium Niobate Electrooptical Modulator. *J. Light. Technol.* **2008**, *26*, 286–290. [CrossRef]
29. Li, J.-Y.; Lu, D.-F.; Qi, Z.-M. Analyses of Wavelength Dependence of the Electro-Optic Overlap Integral Factor for LiNbO₃ Channel Waveguides. *Acta Phys. Sin.* **2014**, *63*, 077801.
30. Song, Y.; Li, W.; Xu, X.; Gao, F.; Song, N. Cold Atoms Guidance into Anti-Resonant Hollow-Core Fibers. *Chin. J. Sci. Instrum.* **2023**, *44*, 127–134.
31. Steck, D.A. Rubidium 87 D Line Data. **2023**, <https://steck.us/alkalidata> (accessed on 26 April 2024)
32. Dotsenko, I.; Alt, W.; Kuhr, S.; Schrader, D.; Müller, M.; Miroshnychenko, Y.; Gomer, V.; Rauschenbeutel, A.; Meschede, D. Application of Electro-Optically Generated Light Fields for Raman Spectroscopy of Trapped Cesium Atoms. *Appl. Phys. B* **2004**, *78*, 711–717. [CrossRef]
33. Wu, X.; Zi, F.; Dudley, J.; Bilotta, R.J.; Canoza, P.; Müller, H. Multiaxis Atom Interferometry with a Single-Diode Laser and a Pyramidal Magneto-Optical Trap. *Optica* **2017**, *4*, 1545. [CrossRef]

34. Moler, K.; Weiss, D.S.; Kasevich, M.; Chu, S. Theoretical Analysis of Velocity-Selective Raman Transitions. *Phys. Rev. A* **1992**, *45*, 342–348. [[CrossRef](#)] [[PubMed](#)]
35. Habib, M.S.; Antonio-Lopez, J.E.; Markos, C.; Schülzgen, A.; Amezcua-Correa, R. Single-Mode, Low Loss Hollow-Core Anti-Resonant Fiber Designs. *Opt. Express* **2019**, *27*, 3824. [[CrossRef](#)] [[PubMed](#)]
36. Kasevich, M.; Weiss, D.S.; Riis, E.; Moler, K.; Kasapi, S.; Chu, S. Atomic Velocity Selection Using Stimulated Raman Transitions. *Phys. Rev. Lett.* **1991**, *66*, 2297–2300. [[CrossRef](#)] [[PubMed](#)]
37. He, M.; Chen, X.; Fang, J.; Chen, Q.; Sun, H.; Wang, Y.; Zhong, J.; Zhou, L.; He, C.; Li, J.; et al. The Space Cold Atom Interferometer for Testing the Equivalence Principle in the China Space Station. *NPJ Microgravity* **2023**, *9*, 58. [[CrossRef](#)]
38. Leong, W.S.; Xin, M.; Chen, Z.; Chai, S.; Wang, Y.; Lan, S.Y. Large Array of Schrödinger Cat States Facilitated by an Optical Waveguide. *Nat. Commun.* **2020**, *11*, 5295. [[CrossRef](#)]

Disclaimer/Publisher’s Note: The statements, opinions and data contained in all publications are solely those of the individual author(s) and contributor(s) and not of MDPI and/or the editor(s). MDPI and/or the editor(s) disclaim responsibility for any injury to people or property resulting from any ideas, methods, instructions or products referred to in the content.